ADVANCED FUNCTIONAL MATERIALS
www.afm-journal.de

High Surface Area MoS_2/Graphene Hybrid Aerogel for Ultrasensitive NO_2 Detection

*Hu Long, Anna Harley-Trochimczyk, Thang Pham, Zirong Tang, Tielin Shi, Alex Zettl, Carlo Carraro, Marcus A. Worsley, and Roya Maboudian**

A MoS_2/graphene hybrid aerogel synthesized with two-dimensional MoS_2 sheets coating a high surface area graphene aerogel scaffold is characterized and used for ultrasensitive NO_2 detection. The combination of graphene and MoS_2 leads to improved sensing properties with the graphene scaffold providing high specific surface area and high electrical and thermal conductivity and the single to few-layer MoS_2 sheets providing high sensitivity and selectivity to NO_2. The hybrid aerogel is integrated onto a low-power microheater platform to probe the gas sensing performance. At room temperature, the sensor exhibits an ultralow detection limit of 50 ppb NO_2. By heating the material to 200 °C, the response and recovery times to reach 90% of the final signal decrease to <1 min, while retaining the low detection limit. The MoS_2/graphene hybrid also shows good selectivity for NO_2 against H_2 and CO, especially when compared to bare graphene aerogel. The unique structure of the hybrid aerogel is responsible for the ultrasensitive, selective, and fast NO_2 sensing. The improved sensing performance of this hybrid aerogel also suggests the possibility of other 2D material combinations for further sensing applications.

1. Introduction

2D layered materials have attracted much attention in recent years due to their remarkable properties and potential for advanced electronic devices.[1,2] Graphene has received much interest since the first report of its exceptional physical properties such as high carrier mobility and excellent mechanical strength.[3] More recently, layered transition-metal dichalcogenides, such as molybdenum disulfide (MoS_2), are being explored as promising alternatives to graphene-based systems for many device applications.[4]

One promising application of 2D materials under investigation is chemical sensing.[1,2] Single-layer graphene has been shown to exhibit excellent sensitivity, at the single molecule level, thanks to its high surface to volume ratio, high electrical conductivity, and low noise.[5–7] Unfortunately, graphene-based sensors without proper surface modification always show poor selectivity.[5–10] Single or few-layer MoS_2 has recently been explored as a potential sensing material for gases such as nitrogen dioxide.[11–21] Nitrogen dioxide (NO_2), one of the most common and toxic air pollutants from combustion and automotive emissions, can cause serious diseases such as chronic bronchitis, emphysema, and respiratory irritation at low concentrations (53 ppb set by the U.S. Environmental Protection Agency).[22–25] Therefore, it is crucially important to develop high performance sensors that are capable of detecting low concentrations of NO_2 in air accurately, reliably, and quickly for human health protection and air-quality monitoring. The promising features of single- and few-layer MoS_2, including improved selectivity compared to graphene, make this material an exciting candidate for this application. However, both graphene- and MoS_2-based field-effect transistor sensors have slow response and recovery times or even no recovery when used at room temperature, which greatly hinders their practical use.[11–20] Faster response and recovery can be achieved by heating the sensing material, which increases the desorption rate of the adsorbed species. In order to keep the sensor power consumption low, a microfabricated heater is typically used for the heating.[10,20,26–29] But integration of single-layer materials onto a microfabricated heater platform can be difficult and the surface area is limited to the heater footprint. The assembly of

H. Long, A. Harley-Trochimczyk, Dr. C. Carraro, Prof. R. Maboudian
Department of Chemical and Biomolecular Engineering
Berkeley Sensor & Actuator Center
University of California, Berkeley
Berkeley, CA 94720, USA
E-mail: maboudia@berkeley.edu
T. Pham, Prof. A. Zettl
Department of Physics
University of California, Berkeley
Materials Sciences Division
Lawrence Berkeley National Laboratory
Kavli Energy NanoSciences Institute
University of California, Berkeley and the Lawrence Berkeley National Laboratory
Berkeley, CA 94720, USA
H. Long, Prof. Z. Tang, Prof. T. Shi
State Key Laboratory of Digital Manufacturing Equipment and Technology
Huazhong University of Science and Technology
Wuhan 430074, China
Dr. M. A. Worsley
Physical and Life Science Directorate
Lawrence Livermore National Laboratory
7000 East Avenue, Livermore, CA 94550, USA

DOI: 10.1002/adfm.201601562

2D sheets into a 3D aerogel structure may open up new opportunities for enhanced sensing properties by maintaining a high surface area in an accessible porous network.[30–32]

Previous efforts to construct aerogels from MoS_2 sheets resulted in a fairly low specific surface area (18 $m^2 g^{-1}$),[33] especially compared to that of graphene aerogel (GA; 1200 $m^2 g^{-1}$).[30–32] A hybrid aerogel with a graphene scaffold coated in single- to few-layer MoS_2 nanosheets leverages the complementary properties of the two materials.[33–35] 3D MoS_2/graphene hybrid structures have been investigated for hydrogen evolution catalysis,[33,35–38] supercapacitors,[39] lithium storage,[40] and DNA sensing.[41] To date, the use of MoS_2/graphene hybrid structure for gas sensing has not been reported. For conductometric sensing purposes, the graphene scaffold allows for lower noise measurements than MoS_2 alone, since MoS_2 is much less conductive than graphene.[33] Furthermore, the thermal conductivity of graphene is much higher than MoS_2 (5000 vs 35 W m^{-1} K^{-1} for single layer),[42,43] thus the graphene scaffold can efficiently and quickly distribute heat from the microheater platform to the MoS_2 sheets. The 2D structure of the MoS_2 sheets on graphene not only increases the contact area for efficient charge transfer across the interface but also shortens the charge transport time and distance, thereby improving the device performance.[4,34,35]

Here we report, for the first time, the use of high surface area MoS_2/graphene hybrid aerogel (MoS_2/GA) for the selective detection of NO_2 at ultralow concentrations with fast response and recovery times. Benefiting from its large surface area, porous structure, and high electrical conductivity, this hybrid aerogel exhibits superior sensing performance for NO_2 detection. The NO_2 sensor is realized by integrating the novel 3D hybrid aerogel on a low-power microheater platform. The detection limit of the sensor is below 50 ppb NO_2 at both room temperature (≈0.1 mW power consumption) and 200 °C (≈4 mW power consumption). At 200 °C, the sensor shows much-improved response and recovery times (<1 min) compared to room temperature, while maintaining low power consumption, thus greatly expanding the practical application of this sensor.

2. Results and Discussion

2.1. Synthesis and Characterization of MoS_2/Graphene Hybrid Aerogel

Figure 1 shows a schematic of the MoS_2/GA synthesis process. First, an electrically conductive, highly crystalline, and mechanically robust GA with ultra high surface area is prepared according to a method reported previously.[30–32] Graphene oxide sheets are cross-linked, dried using supercritical CO_2, and annealed at high temperature to obtain the graphene aerogel (Figure 1a). To create the MoS_2/graphene hybrid aerogel, the GA is immersed in an aqueous solution of ammonium thiomolybdate (ATM), freeze-dried, and then annealed at 450 °C under 2% H_2/Ar (Figure 1b,c).[33] To ensure that the ATM precursor is fully reduced to MoS_2, the MoS_2/GA sample is further treated with a two-step annealing process in the presence of sulfur.

The morphology of the MoS_2/GA is characterized with scanning electron microscopy (SEM) and high-resolution transmission electron microscopy (HRTEM). SEM images of the as-synthesized MoS_2/GA (**Figure 2**a,b) show that the hybrid aerogel has the form of continuous 3D assemblies with thin interconnected sheets. The hybrid aerogel maintains the porous features of the bare GA, as seen in Supporting Information Figure S1. The average pore size of the hybrid aerogel is around 6 nm.[33] The open porous network of the MoS_2/GA allows the aerogel surface area to be readily accessed and facilitates gas diffusion. In the HRTEM analysis, shown in Figure 2d,e, the graphene and MoS_2 can be clearly distinguished from their lattice spacings (0.35 nm[44] vs 0.65 nm,[4] respectively). The analysis indicates that most of the graphene scaffold is coated on both sides with MoS_2, which is present in the form of one to three-layer sheets (mainly monolayer); thus, the benefits of the 2D material are preserved in this 3D structure. The selected-area electron diffraction (SAED) pattern is shown in Figure 2f with several diffraction rings, which can be indexed to the planes of hexagonal-phase MoS_2 (M) and graphene (G) sheets. The uniform distribution of MoS_2 on the graphene scaffold is confirmed

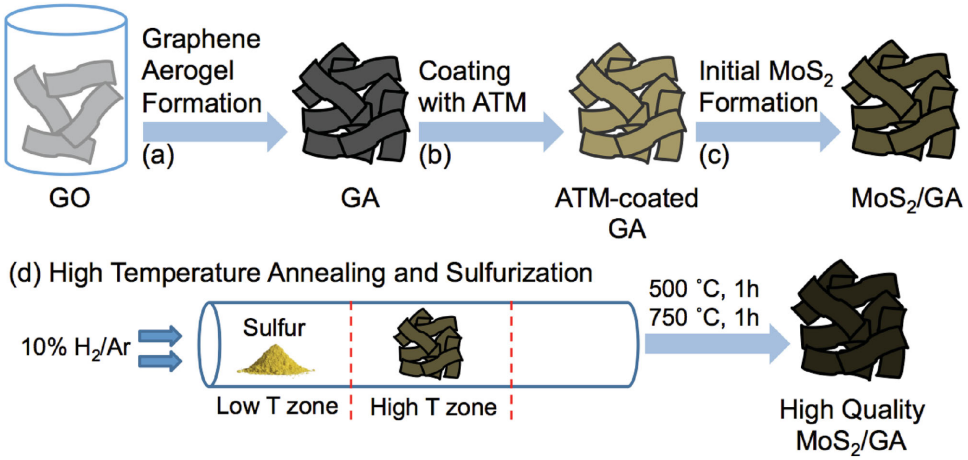

Figure 1. Schematic illustration of the synthesis process for MoS_2/graphene aerogel. a) Graphene oxide (GO) sheets are cross-linked, supercritically dried, and annealed at high temperature to form graphene aerogel (GA). b) GA is soaked in a solution of ammonium thiomolybdate (ATM) and freeze-dried. c) ATM-coated GA is annealed at 450 °C in 2% H_2/Ar for 4 h. d) Two-step high temperature annealing (at 500 and 750 °C) for 1 h each in 10% H_2/Ar with excess sulfur improves the quality of the final MoS_2/GA aerogel.

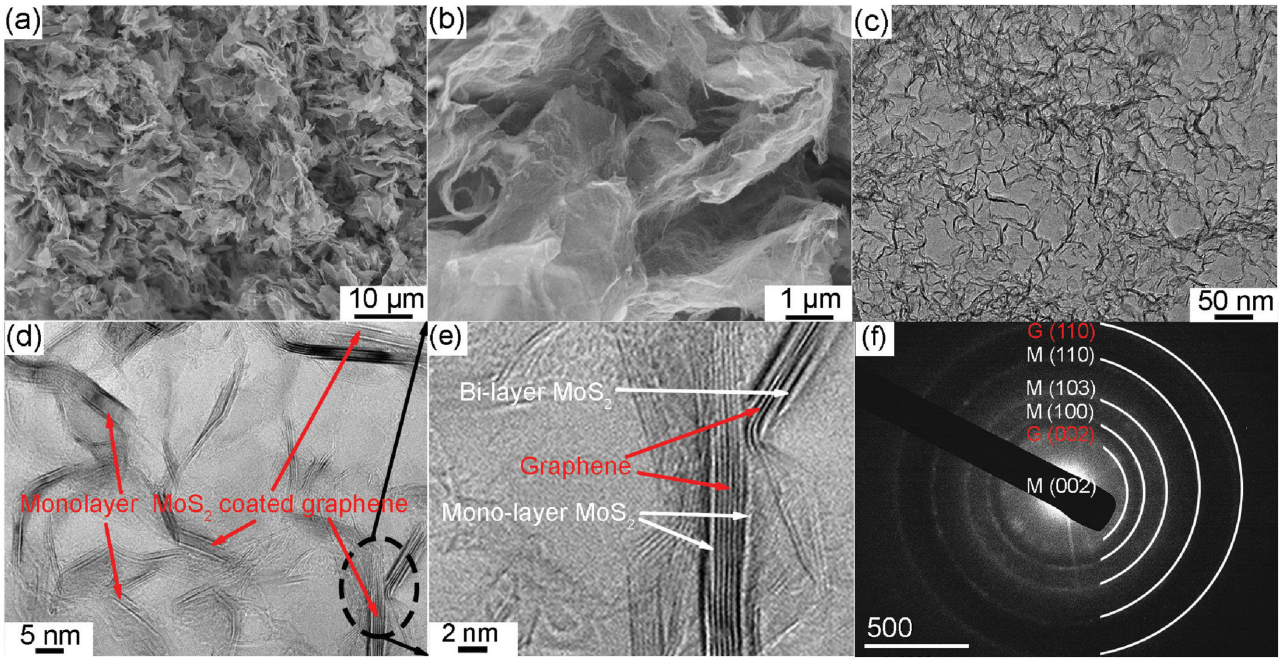

Figure 2. Morphology of the as-prepared MoS_2/GA. a,b) SEM images of the hybrid aerogel with different magnifications. c) Low magnification TEM image of the MoS_2/GA. d) High resolution TEM image of the MoS_2/GA, showing most of the graphene is coated by monolayer MoS_2. e) Enlarged TEM image demonstrating the MoS_2 coating of the few-layer graphene scaffold. f) Relevant selected area electron diffraction (SAED) pattern of the MoS_2/GA.

by energy-dispersive X-ray spectroscopy (EDX) elemental maps shown in Figure S2 (Supporting Information), where C, Mo, and S are seen to be uniformly distributed throughout the hybrid aerogel. Because the graphene aerogel is conformally coated with single and few-layer MoS_2, the hybrid structure possesses high surface area (700 $m^2 g^{-1}$),[33] an important characteristic for sensing. For comparison, MoS_2 aerogel is also synthesized by a similar procedure. Without the 3D graphene framework as a scaffold, the MoS_2 aerogel has an aggregated morphology (nanoparticles) as shown in Figure S3 (Supporting Information) and a much lower specific surface area (18 $m^2 g^{-1}$).[33]

Raman spectra, shown in **Figure 3**a,b, show the characteristic peaks of MoS_2 and graphene. The major peaks associated with MoS_2 are at 378 and 407 cm^{-1} and correspond to the in-plane E^1_{2g} and out-of-plane A^1_g vibrational modes of hexagonal MoS_2, respectively, in good agreement with literature values for multilayer MoS_2. Two strong peaks observed at 1357 and 1589 cm^{-1} match well with the D and G bands of graphene. X-ray photoelectron spectroscopy (XPS) is used to further study the surface electronic state and composition of MoS_2/GA. Sulfur, molybdenum, carbon, and oxygen peaks are clearly identified in the survey spectrum in Figure S4 (Supporting Information) and the high-resolution scans in Figure 3c–f. The S 2p region shows two characteristic peaks located at 162.0 and 163.1 eV corresponding to S $2p_{3/2}$ and S $2p_{1/2}$, respectively, which can be indexed to Mo—S bonding in MoS_2. Surprisingly, the Mo peaks show two Mo oxidation states (Mo^{4+} and Mo^{6+}), which can be indexed to the Mo—S and the Mo—O bonding, respectively. The calculated S:Mo (Mo^{4+} and Mo^{6+}) ratio is 2.4, whereas when only the Mo^{4+} is used, the S:Mo ratio is 10:1, which suggests it is unlikely that Mo is in a separate molybdenum oxide phase. This is consistent with the absence of molybdenum oxide peaks in Raman spectra. Additionally, the carbon peak (Figure 3e) can be deconvoluted into two peaks, a large peak at 284.6 eV attributed to C—C bonding environment associated with the graphene scaffold, and a smaller peak at 286.0 eV attributed to C—O bonding which indicates that Mo—O does not come from a MoO_3 phase, but rather from a Mo—O—C bonding environment at the interface between MoS_2 and graphene. The O 1s region (Figure 3f) exhibits three peaks. In addition to the peak at 532.6 eV that is commonly observed in ex situ analyzed samples, there is a peak at 530.5 eV that can be assigned to Mo—O bonding and a peak at 530.9 eV that can be assigned to C—O bonding, which further corroborates the Mo—O—C bonding. The formation of a Mo—O bond without Mo—S scission has been reported elsewhere,[45–47] and suggests strong chemical and electronic coupling between the MoS_2 and graphene in the synthesized aerogel. This unique Mo environment with O- and S-bonding may offer more active defect sites as well as unusual electronic properties.[45,47] Based on the morphological and compositional characterizations described above, the MoS_2/GA displays a high surface area with a uniform distribution of few-layer MoS_2 sheets that are covalently bonded to the graphene scaffold.

2.2. Sensor Fabrication

The synthesized MoS_2/graphene aerogel is evaluated for NO_2 sensing by integrating it onto a low power microheater platform. **Figure 4**a shows a cross-sectional schematic of the sensor. The microheater consists of a polycrystalline silicon (Poly-Si) microheater embedded in a low-stress silicon nitride (LSN) membrane with Pt/Ti metal contacts for the microheater and the sensing material. Figure S5 (Supporting Information)

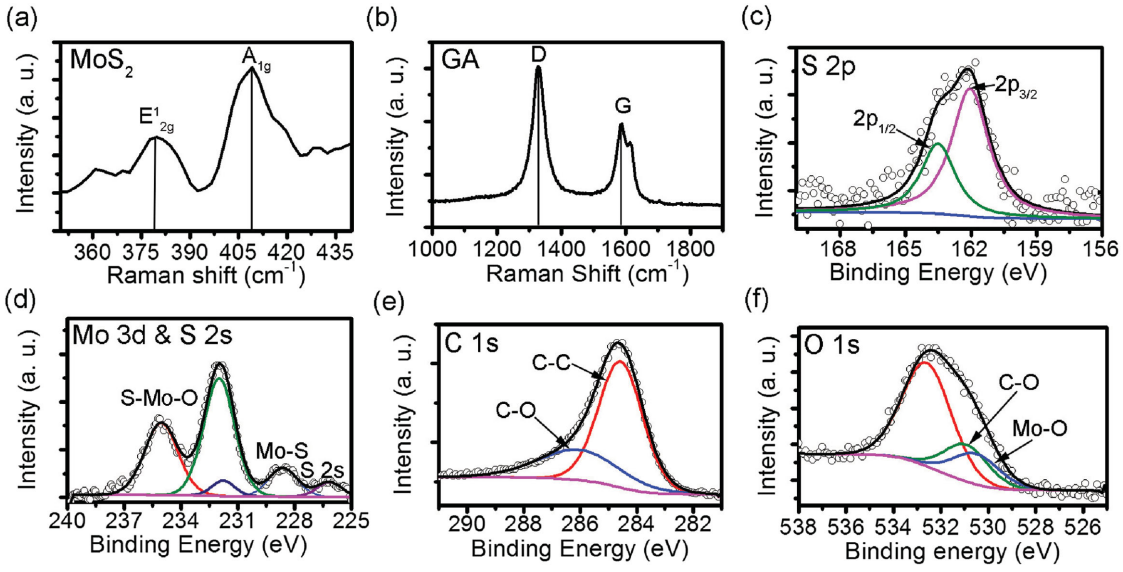

Figure 3. a,b) Raman spectra of the hybrid aerogel. X-ray photoelectron spectra of the MoS_2/graphene hybrid aerogel: c) S 2p; d) Mo 3d and S 2s; e) C 1s; f) O 1s.

shows a real color optical image of the 3.5 × 3.5 mm^2 chip containing four microheater sensors. Figure 4b shows a zoomed-in view of a single microheater device showing the two platinum sensor electrodes (yellow) above the microheater (green) embedded in the LSN membrane (purple). Full fabrication details and heater characterization can be found elsewhere.[26,27] The membrane thermally isolates the heated sensing area and minimizes heat lost through conduction to the silicon substrate. With this design, the heater consumes only 15 mW to reach 700 °C. Besides the low power consumption, the microheater platform has excellent stability in the temperature range of interest and a closed membrane configuration to make sensing material deposition easier. The aerogel is sonicated into suspension in a solution of de-ionized water and isopropyl alcohol and drop-cast onto the microheater while the heater is powered to 3 mW (≈100 °C) to drive localized deposition.

2.3. Gas Sensing Performance

The sensor exhibits a linear current–voltage response. Figure 4c shows a typical gas sensor response curve at room temperature toward different NO_2 concentrations, from 50 ppb to 5 ppm, at a bias voltage of 0.5 V. Upon exposure to NO_2, the sensor resistance exhibits a pronounced decrease. The sensing mechanism relies on the direct charge transfer between NO_2 and MoS_2/GA. Nitrogen dioxide is a known electron acceptor due to the unpaired electron on the nitrogen atom. Upon NO_2 adsorption, since the electron extraction from MoS_2/GA is causing a decrease in sensor resistance, the aerogel is exhibiting a p-type characteristic. During subsequent exposure to clean air, the sensor resistance slowly recovers as NO_2 molecules desorb from the surface. This behavior is consistent with the charge transfer mechanism of single-layer graphene,[7] MoS_2,[15] and carbon nanotube gas sensors.[22] However, understanding the complete mechanism is a complex subject in gas sensing studies because of the combined effects of physisorption, chemisorption, the role of defect sites, and the transduction mechanism.[17] As reported for reduced graphene oxide and few-layer MoS_2 sensors, the adsorption of gas can be divided into two parts, adsorption on low energy binding sites (such as sp^2 bonded carbon) and on high energy binding sites (defects including vacancies and functional groups).[11] The low energy

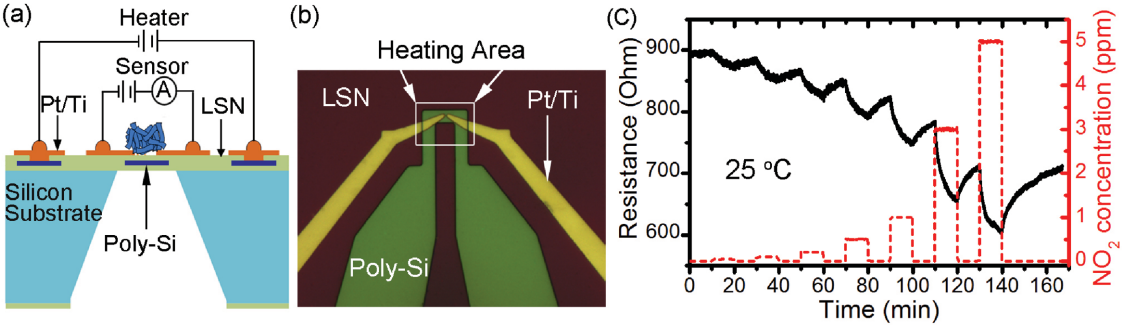

Figure 4. a) Cross-sectional schematic of the microheater sensor. b) Optical image of one microheater showing the Pt/Ti sensing electrodes above the polysilicon heater. c) Real time response of the sensor at room temperature toward different NO_2 concentrations.

binding sites induce a rapid response through weak dispersive forces, while the high energy sites allow slow but strong binding.[48] As seen in Figure 4c, the slow rates of response and recovery at room temperature suggest defect-dominated adsorption. The S—Mo—O bonds and the excess sulfur, based on the XPS analysis, may be the source of these defects. The defect sites explain the high sensitivity even for very low concentrations of gas. In Figure 4c, a clear response is visible even at a NO_2 concentration of 50 ppb (the lowest concentration that can be accurately delivered by the gas delivery system), which is lower than most single- or few-layer MoS_2 transistor-based sensors (Table S1, Supporting Information). Given the size of the response to 50 ppb, it is expected that the sensor would respond to even lower concentrations of NO_2.

At room temperature, the response and recovery rates are slow, because of the strong adsorption of NO_2 on MoS_2 surface, which is also observed in carbon nanotube,[22,49] graphene,[9,10] and MoS_2[13,15,18] sensors. Incomplete recovery of the sensor leads to an unreliable sensing output in practical applications. Heating the sensing material with a microfabricated heater can enhance the reversibility of the sensor and accelerate the response and recovery rates, while maintaining low power consumption.[26–29] **Figure 5**a shows the sensor response to 0.5 ppm NO_2 at various heating temperatures, ranging from room temperature to 200 °C. The sensor response is presented as $(R_{gas} - R_{air})/R_{air}$, where R_{air} and R_{gas} represent the resistance of the device to air and NO_2 gas, respectively. At 200 °C (with the microheater consuming ~4 mW), the sensor shows fast response and complete recovery. The magnitude of the sensor response to NO_2 is, however, slightly smaller at high temperature than at low temperature. This behavior is consistent with the proposed sensing mechanism. At low temperature, the adsorption of NO_2 is substantial and continues during the gas exposure, while desorption is negligible due to the strong bonding between NO_2 and MoS_2/GA. An equilibrium between adsorption and desorption is not reached within a practical timeframe and the sensor resistance decreases as NO_2 coverage continues to increase. The NO_2 desorption is enhanced at higher temperature, which speeds up the time to reach a balance between adsorption and desorption both during gas exposure and during recovery. Although the response and recovery times might be even faster at higher temperature, 200 °C provides an effective temperature when also considering the sensor power consumption.

The sensor is further tested at 200 °C against different NO_2 concentrations, from 50 ppb to 1 ppm. As shown in Figure 5b, the sensor shows increased response at higher NO_2 concentrations. Response and recovery times for all NO_2 concentrations are fast. The average time to reach 90% of the stable sensor signal (t_{90}) is 21.6 s for response and 29.4 s for recovery. The sensor shows clear response to 50 ppb NO_2 with fast response and nearly complete recovery and a signal-to-noise ratio of about 11. By using a signal-to-noise threshold of 3, the calculated detection limit of the sensor is 14 ppb NO_2. Compared to other graphene- and MoS_2-based NO_2 sensors listed in Table S1 (Supporting Information), the sensor presented shows superior sensing performance such as low detection limit, fast response and recovery, and low power consumption.

Figure 5c is a plot of sensor response versus NO_2 concentrations, displaying a nonlinear relationship between the gas

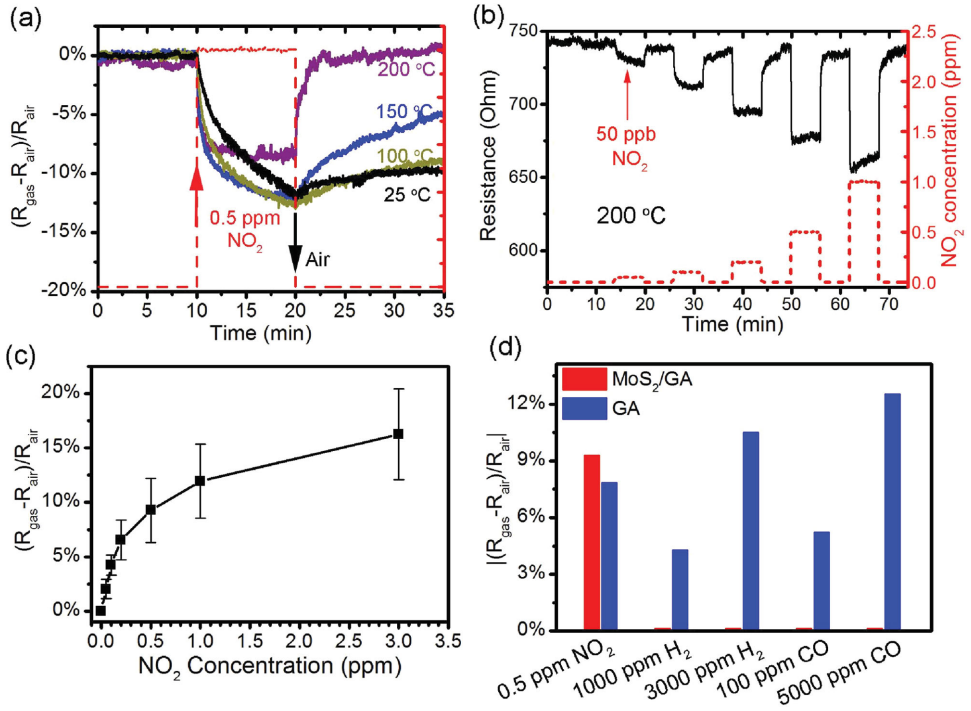

Figure 5. a) Sensor response to 0.5 ppm NO_2 at various microheater temperatures, displaying improvement in response and recovery time. b) Real-time resistance change of the sensor with the microheater temperature of 200 °C. c) Response versus NO_2 concentration for microheater temperature of 200 °C. d) Selectivity of the MoS_2/GA sensor compared to GA alone for microheater temperature of 200 °C.

concentration and the sensor response. Assuming the gas adsorption is dominated by high-energy defect sites, at low NO_2 concentrations when most of the sites are available, the charge transfer is directly proportional to the gas concentration. At higher NO_2 concentrations, the sites may eventually all be occupied during the gas exposure, and thus the response reaches a saturation point. However, in the experimental concentration range, the response does not saturate completely. Robinson et al. have suggested that additional gas molecules may cluster at an already populated defect site, contributing to a small amount of charge transfer that would continue to decrease the resistance.[48,49]

In order to better assess the benefit of the MoS_2 coating, the NO_2 sensing performance with pure graphene aerogel was probed. As seen in Figure 5d, the GA sensor has similar NO_2 sensing response as the MoS_2/GA while exhibiting a higher detection limit of 100 ppb, but the selectivity is much improved with the addition of MoS_2. The MoS_2/GA and bare GA sensors are exposed to high concentration of typical toxic and combustible gases, carbon monoxide (CO) and hydrogen (H_2). While the GA responds to all of the tested gases, the MoS_2/GA only responds to NO_2, even though the concentration is much lower. Previous theoretical study shows that NO_2 possesses the largest binding energy compared to CO and H_2 when adsorbed on MoS_2.[50] This is likely the reason why the MoS_2/GA hybrid has good selectivity against CO and H_2. In addition, the extra S in the structure may provide improved selectivity due to the possibility for increased number of bridging S atoms at the edges of MoS_2.[51] Further study is needed to more fully understand the mechanism behind the selectivity reported here.

3. Conclusion

In summary, we have synthesized a high-surface area 3D MoS_2/graphene hybrid aerogel and demonstrated its effectiveness as a sensing material for NO_2 utilizing a low-power microheater platform. The high-quality graphene aerogel serves as the scaffold, which provides the high specific surface area, porosity, and high electrical and thermal conductivity. The graphene scaffold is covered with single to few-layer MoS_2 sheets, which provide the sensitive and selective sensing performance. The hybrid aerogel is integrated onto a low-power microheater platform for NO_2 sensing evaluation. The sensor exhibits an ultralow detection limit of 50 ppb NO_2 at both room temperature and 200 °C. By heating the material to 200 °C, a fast response and recovery of the sensor (<1 min) is achieved, which greatly expands the practical application of the sensor. The MoS_2/GA shows good selectivity against H_2 and CO, especially when compared to bare GA. The improved detection limit, sensitivity, and selectivity can be attributed to the unique structure of the hybrid aerogel. The porous 3D structure of the aerogel makes it highly accessible to the target gas. The bonding between the MoS_2 and graphene results in strong electronic coupling and the excess sulfur creates defects that improve the sensitivity of the sensor. The MoS_2/GA aerogel leverages the properties of the two materials to result in a high performance hybrid material for ultrasensitive and fast NO_2 sensing and suggests the possibility of other 2D material combinations for improved sensing applications.

4. Experimental Section

Material Synthesis: High-quality GA was synthesized according to our previous reported method.[30–35] In a typical process, 3 mL of an aqueous graphene oxide suspension (2 wt% graphene oxide) was mixed with 500 µL concentrated ammonium hydroxide (NH_4OH). The vial was sealed and placed in an oven at 85 °C for 12 h. The resulting wet gel was washed in deionized water to remove the NH_4OH. This was followed by an exchange of water with acetone inside the pores. Supercritical CO_2 was used to dry the gel that was then converted to the graphene aerogel by pyrolysis at 1050 °C under nitrogen for 3 h. The GA was subjected to an additional thermal annealing at 2000 °C in He to improve the graphene crystallinity. For MoS_2 coating, the GA was immersed in 1 mol L^{-1} ammonium thiomolybdate solution and submerged in liquid nitrogen for rapid freezing and further freeze-drying. The ATM coated aerogel was annealed in 2% H_2/Ar mixture at 450 °C for 4 h to yield the MoS_2/GA aerogel. To further improve the MoS_2 quality, the aerogel was annealed by a two-step annealing process. First, the aerogel was placed in the hot zone (T_H) of a low-pressure furnace (base pressure of 700 mTorr) while sulfur was placed in the upstream low-temperature (T_L) zone of the furnace. With a 10% H_2/Ar mixture flowing continuously through the tube, the aerogel was first heated at T_H = 500 °C for 1 h to reduce any possible MoO_3 into MoO_2. At this furnace set-point, the low-temperature zone was at T_L < 113 °C. The furnace was then heated to T_H = 750 °C for 1 h, at which point the low-temperature zone reached 120 °C (above the melting point of sulfur) and sulfur vapor reacted with the aerogel to fully sulfurize the molybdenum. The furnace was cooled back down to room temperature under continued H_2/Ar flow.

Material Characterization: The morphology of the high-quality MoS_2/graphene aerogel was characterized using a JEOL JSM-6700F field-emission SEM operated at 5 keV with a working distance of 8 mm, a JEOL 7401-F field-emission SEM equipped with EDX analyzer operated in lower secondary electron imaging mode at 10 keV (20 mA), and a JEOL 2010 HRTEM operated at 80 keV. XPS measurements were carried out on an Omicron Dar400 system with an achromatic Al K_a X-ray source.

Microheater Sensor Fabrication: Microheaters were fabricated using 4-mask surface micromachining process to create a polycrystalline silicon microheater embedded in a thin silicon nitride membrane. The fabrication details can be found in our previous reports.[26,27] Briefly, 100 nm in situ doped poly-Si was patterned and encapsulated in 200 nm LSN film. Sensing electrodes as well as contact to the microheaters was made by patterning and subsequent deposition of 10 nm of titanium and 90 nm of platinum. Finally, the wafers were patterned and KOH etched from the backside to remove the silicon under the microheaters leaving only the thin silicon nitride membrane. The wafer was then diced into 3.5 mm × 3.5 mm chips, which typically contain four individual microheaters per chip. The microheaters used in this work are 10 µm wide, 100 nm long, and 100 nm thick. Once individualized, the microheater chips were wire-bonded into a 14-pin cer-dip package for electrical characterization and the voltage was controlled with a Keithley 2602A sourcemeter. The as-synthesized MoS_2/GA was sonicated into suspension and deposited from a solution of de-ionized water and isopropyl alcohol. A 0.25 µL drop of 1 mg mL^{-1} solution was placed on the microheater chip while the microheater was powered to 3 mW (100 °C). Heating the microheater promoted solvent evaporation and led to materials deposited at the center of the microheater.

Gas Delivery: The microheater cer-dip package was placed within a gas flow chamber with a volume of 1 cm^3. The sensor was exposed to NO_2 using a computer-controlled gas delivery system. A cylinder of 20 ppm NO_2 gas balanced in nitrogen was used (Praxair). For selectivity tests, sensors were exposed to various concentrations of CO (Praxair, 5000 ppm in N_2), and hydrogen (Praxair, 5% in N_2) using the same gas delivery system. Sensor testing was performed at a constant flow rate of 300 sccm. Stream balance and purge was made up of house air that had passed through pressure swing adsorption dryers to remove humidity and an activated carbon scrubber to remove other contaminants. Mass flow controllers (Bronkhorst) controlled by LabView were used to dilute

the gas mixture cylinder with clean air and deliver these gases to the sensor chamber. Flow stream temperatures were recorded and were within a few degrees of room temperature.

Sensor Measurement: The measurement of the microheater sensor was performed using a Keithley 2602 sourcemeter. The sourcemeter was controlled using Zephyr, an open-source Java-based instrument and control and measurement software suite. Zephyr was also used to acquire data from the sourcemeter, the gas delivery system, such as flow rates and concentrations, and any reference sensors, such as temperature and humidity sensors. The microheater sensors were measured by continuously applying a bias voltage. The current through the sensor was recorded and its resistance, R, was calculated. The sensor response was determined by the relative change in resistance, which was defined as $(R_{gas} - R_{air})/R_{air}$, where R_{gas} is the resistance during exposure to given gas concentration and R_{air} is the average resistance in clean air before any gas exposure.

Supporting Information

Supporting Information is available from the Wiley Online Library or from the author.

Acknowledgements

The authors acknowledge Lunet Luna for help with material characterization. This work was supported by Berkeley Sensor and Actuator Center (BSAC) Industrial Members and National Science Foundation (NSF Grant No. IIP 1444950), which provided the design of experiments, student support (H.L., A.H.-T.), and sensor fabrication and performance characterization. The SEM and EDS characterizations were conducted at the Molecular Foundry, which is supported by the Office of Science, Office of Basic Energy Sciences, of the U.S. Department of Energy under Contract No. DE-AC02-05CH11231. T.P. and A.Z. acknowledge funding from the Director, Office of Basic Energy Sciences, Materials Sciences and Engineering Division of the U.S. Department of Energy under Contract No. DE-AC02-05CH11231, under the sp^2 program (KC2207), which provided TEM characterization; and the Air Force Office of Scientific Research under contract FA9550-14-1-0323, which provided student (T.P.) support and synthesis route optimization. M.W. would like to acknowledge that this work was supported by Lawrence Livermore National Laboratory under the auspices of the U.S. Department of Energy under Contract DE-AC52-07NA27344, through LDRD award 13-LW-099. H.L. and A.H.-T. acknowledge additional support through the China Scholarship Council and the NSF Graduate Research Fellowship (DGE 1106400).

Received: March 28, 2016
Published online: May 23, 2016

[1] A. K. Geim, K. S. Novoselov, *Nat. Mater.* **2007**, *6*, 183.
[2] S. Z. Butler, S. M. Hollen, L. Cao, Y. Cui, J. A. Gupta, H. R. Gutierrez, T. F. Heinz, S. S. Hong, J. Huang, A. F. Ismach, E. Johnston-Halperin, M. Kuno, V. V. Plashnitsa, R. D. Robinson, R. S. Ruoff, S. Salahuddin, J. Shan, L. Shi, M. G. Spencer, M. Terrones, W. Windl, J. E. Goldberger, *ACS Nano* **2013**, *7*, 2898.
[3] K. S. Novoselov, A. K. Geim, S. V. Morozov, D. Jiang, Y. Zhang, S. V. Dubonos, I. V. Griorieva, A. A. Firsov, *Science* **2004**, *306*, 666.
[4] B. Radisavljevic, A. Radenovic, J. Brivio, V. Giacometti, A. Kis, *Nat. Nanotechnol.* **2011**, *6*, 147.
[5] F. Schedin, A. K. Geim, S. V. Morozov, E. W. Hill, P. Blake, M. I. Katsnelson, K. S. Novoselov, *Nat. Mater.* **2007**, *6*, 652.
[6] T. O. Wehling, K. S. Novoselov, S. V. Morozov, E. E. Vdovin, M. I. Katsnelson, A. K. Geim, A. I. Lichtenstein, *Nano Lett.* **2008**, *8*, 173.
[7] W. Li, X. Geng, Y. Guo, J. Rong, Y. Gong, L. Wu, X. Zhang, P. Li, J. Xu, G. Cheng, M. Sun, L. Liu, *ACS Nano* **2011**, *5*, 6955.
[8] A. K. Geim, *Science* **2009**, *324*, 1530.
[9] J. D. Fowler, M. J. Allen, V. C. Tung, Y. Yang, R. B. Kaner, B. H. Weiller, *ACS Nano* **2009**, *3*, 301.
[10] H. Choi, J. S. Choi, J. Kim, J. Choe, K. H. Chung, J. Shin, J. T. Kim, D. Youn, K. Kim, J. Lee, S. Choi, P. Kim, C. Choi, Y. Yu, *Small* **2014**, *10*, 3685.
[11] H. Li, Z. Yin, Q. He, H. Li, X. Huang, G. Lu, D. W. H. Fam, A. I. Y. Tok, Q. Zhang, H. Zhang, *Small* **2012**, *8*, 63.
[12] Q. He, Z. Zeng, Z. Yin, H. Li, S. Wu, X. Huang, H. Zhang, *Small* **2012**, *8*, 2994.
[13] D. J. Late, Y.-K. Huang, B. Liu, J. Acharya, S. N. Shirodkar, J. Luo, A. Yan, D. Charles, U.V. Waghmare, V. P. Dravid, C. N. R. Rao, *ACS Nano* **2013**, *7*, 4879.
[14] Y. Yao, L. Tolentino, Z. Yang, X. Song, W. Zhang, Y. Chen, C. Wong, *Adv. Funct. Mater.* **2013**, *23*, 3577.
[15] K. Lee, R. Gatensby, N. McEvoy, T. Hallam, G. S. Duesberg, *Adv. Mater.* **2013**, *25*, 6699.
[16] F. K. Perkins, A. L. Friedman, E. Cobas, P. M. Campbell, G. G. Jernigan, B. T. Jonker, *Nano Lett.* **2013**, *13*, 668.
[17] J.-S. Kim, H.-W. Yoo, H. O. Choi, H.-T. Jung, *Nano Lett.* **2014**, *14*, 5941.
[18] B. Cho, M. G. Hahm, M. Choi, J. Yoon, A. R. Kim, Y.-J. Lee, S.-G. Park, J.-D. Kwon, C. S. Kim, M. Song, Y. Jeong, K.-S. Nam, S. Lee, T. J. Yoo, C. G. Kang, B. H. Lee, H. C. Ko, P. M. Ajayan, D.-H. Kim, *Sci. Rep.* **2015**, *5*, 08052.
[19] B. Cho, A. R. Kim, Y. Park, J. Yoon, Y.-J. Lee, S. Lee, T. J. Yoo, C. G. Kang, B. H. Lee, H. C. Ko, D.-H. Kim, M. G. Hahm, *ACS Appl. Mater. Interfaces* **2015**, *7*, 2952.
[20] M. Donarelli, S. Prezioso, F. Perrozzi, F. Bisti, M. Nardone, L. Giancaterini, C. Cantalini, L. Ottaviano, *Sens. Actuators, B* **2015**, *207*, 602.
[21] R. Samnakay, C. Jiang, S. L. Rumyantsev, M. S. Shur, A. A. Balandin, *Appl. Phys. Lett.* **2015**, *106*, 023115.
[22] J. Kong, N. R. Franklin, C. Zhou, M. G. Chapline, S. Peng, K. Cho, H. J. Dai, *Science* **2000**, *287*, 622.
[23] Y. Shimizu, M. Egashira, *MRS Bull.* **1999**, *24*, 18.
[24] G. Ko, H. Y. Kim, J. Ahn, Y. M. Park, K. Y. Lee, J. Kim, *Curr. Appl. Phys.* **2010**, *10*, 1002.
[25] "Nitrogen Dioxide," Environmental Protection Agency, http://www.epa.gov/airquality/nitrogenoxides/, accessed: Feb. 2015.
[26] A. Harley-Trochimczyk, J. Chang, Q. Zhou, J. Dong, T. Pham, M. A. Worsley, R. Maboudian, A. Zettl, W. Mickelson, *Sens. Actuators, B* **2015**, *206*, 399.
[27] A. Harley-Trochimczyk, T. Pham, J. Chang, E. Chen, M. A. Worsley, A. Zettl, W. Mickelson, R. Maboudian, *Adv. Funct. Mater.* **2016**, *26*, 433.
[28] W. Mickelson, A. Sussman, A. Zettl, *Appl. Phys. Lett.* **2012**, *100*, 173110.
[29] H. Long, A. Harley-Trochimczyk, T. He, T. Pham, Z. R. Tang, T. L. Shi, A. Zettl, W. Mickelson, C. Carraro, R. Maboudian, *ACS Sens.* **2016**, *1*, 339.
[30] M. A. Worsley, P. J. Pauzauskie, T. Y. Olson, J. Biener, J. H. Satcher Jr., T. F. Baumann, *J. Am. Chem. Soc.* **2010**, *132*, 14067.
[31] M. A. Worsley, S. O. Kucheyev, H. E. Mason, M. D. Merrill, B. P. Mayer, J. Lewicki, C. A. Valdez, M. E. Suss, M. Stadermann, P. J. Pauzauskie, J. H. SatcherJr., J. Biener, T. F. Baumann, *Chem. Commun.* **2012**, *48*, 8428.
[32] M. A. Worsley, T. Pham, A. Yan, S. J. Shin, J. R. I. Lee, M. Bagge-Hansen, W. Mickelson, A. Zettl, *ACS Nano* **2014**, *8*, 11013.
[33] M. A. Worsley, S. J. Shin, M. D. Merrill, J. Lenhardt, A. J. Nelson, L. Y. Woo, A. E. Gash, T. F. Baumann, C. A. Orme, *ACS Nano* **2015**, *9*, 4698.

[34] K. Roy, M. Padmanabhan, S. Goswami, T. P. Sai, G. Ramalingam, S. Raghavan, A. Ghosh, *Nat. Nanotechnol.* **2013**, *8*, 826.
[35] Y. Li, H. Wang, L. Xie, Y. Liang, G. Hong, H. Dai, *J. Am. Chem. Soc.* **2011**, *133*, 7296.
[36] Y. Hou, B. Zhang, Z. H. Wen, S. M. Cui, X. R. Guo, Z. He, J. H. Chen, *J. Mater. Chem. A* **2014**, *2*, 13795.
[37] Y. Zhao, X. Xie, J. Zhang, H. Liu, H.-J. Ahn, K. Sun, G. Wang, *Chem. Eur. J.* **2015**, *21*, 15908.
[38] K. Chang, Z. Mei, T. Wang, Q. Kang, S. Ouyang, J. Ye, *ACS Nano* **2014**, *8*, 7078.
[39] K.-J. Huang, L. Wang, J.-Z. Zhang, K. Xing, *J. Electroanal. Chem.* **2015**, *752*, 33.
[40] K. Chang, W. Chen, *ACS Nano* **2011**, *5*, 4720.
[41] P. T. K. Loan, W. Zhang, C.-T. Lin, K.-H. Wei, L.-J. Li, C.-H. Chen, *Adv. Mater.* **2014**, *26*, 4838.
[42] A. A. Balandin, S. Ghosh, W. Bao, I. Calizo, D. Teweldebrhan, F. Miao, C. N. Lau, *Nano Lett.* **2008**, *8*, 902.
[43] R. Yan, J. R. Simpson, S. Bertolazzi, J. Brivio, M. Watson, X. Wu, A. Kis, T. Luo, A. R. H. Walker, H. G. Xing, *ACS Nano* **2014**, *8*, 986.
[44] A. Reina, X. Jia, J. Ho, D. Nezich, H. Son, V. Bulovic, M. S. Dresselhaus, J. Kong, *Nano Lett.* **2009**, *9*, 30.
[45] A. Azcatl, S. McDonnell, K. C. Santosh, X. Peng, H. Dong, X. Qin, R. Addou, G. I. Mordi, N. Lu, J. Kim, M. J. Kim, K. Cho, *Appl. Phys. Lett.* **2014**, *104*, 111601.
[46] E. G. S. Firmiano, A. C. C. Rabelo, J. Dalmaschio, A. N. Pinheiro, E. C. Pereira, W. H. Schreiner, E. R. Leite, *Adv. Energy Mater.* **2014**, *4*, 1301380.
[47] H. Nan, Z. Wang, W. Wang, Z. Liang, Y. Lu, Q. Chen, D. He, P. Tan, F. Miao, X. Wang, J. Wang, Z. Ni, *ACS Nano* **2014**, *8*, 5738.
[48] J. T. Robinson, F. K. Perkins, E. S. Snow, Z. Wei, P. E. Sheehan, *Nano Lett.* **2008**, *8*, 3137.
[49] J. A. Robinson, E. S. Snow, S. C. Badescu, T. L. Reinecke, F. K. Perkins, *Nano Lett.* **2006**, *6*, 1747.
[50] Q. Yue, Z. Shao, S. Chang, J. Li, *Nanoscale Res. Lett.* **2013**, *8*, 425.
[51] K. Chan, C. Tsai, H. A. Hansen, J. K. Nørskov, *ChemCatChem* **2014**, *6*, 1899.